




Cite this: *Nanoscale*, 2017, **9**, 5779

Received 2nd March 2017,  
Accepted 7th April 2017

DOI: 10.1039/c7nr01516j

rsc.li/nanoscale

## Radio frequency negative permittivity in random carbon nanotubes/alumina nanocomposites†

Chuanbing Cheng,<sup>a,c,d</sup> Runhua Fan,<sup>\*a,c</sup> Yanrong Ren,<sup>b</sup> Tao Ding,<sup>\*b</sup> Lei Qian,<sup>c,e</sup> Jiang Guo,<sup>d</sup> Xiaofeng Li,<sup>a</sup> Liqiong An,<sup>a</sup> Yanhua Lei,<sup>a</sup> Yansheng Yin<sup>a</sup> and Zhanhu Guo  <sup>\*d</sup>

While metal is the most common conductive constituent element in the preparation of metamaterials, one-dimensional conductive carbon nanotubes (CNTs) provide alternative building blocks. Here alumina (Al<sub>2</sub>O<sub>3</sub>) nanocomposites with multi-walled carbon nanotubes (MWCNTs) uniformly dispersed in the alumina matrix were prepared by hot-pressing sintering. As the MWCNT content increased, the formed conductive MWCNT networks led to the occurrence of the percolation phenomenon and a change of the conductive mechanism. Two different types of negative permittivity (*i.e.*, resonance-induced and plasma-like) were observed in the composites. The resonance-induced negative permittivity behavior in the composite with a low nanotube content was ascribed to the induced electric dipole generated from the isolated MWCNTs. The frequency dispersions of such negative permittivity can be fitted well by the Lorentz model, while the observed plasma-like negative permittivity behavior in the composites with MWCNT content exceeding the percolation threshold could be well explained by the low frequency plasmonic state generated from conductive nanotube networks using the Drude model. This work is favorable to revealing the generation mechanism of negative permittivity behavior and will greatly facilitate the practical applications of metamaterials.

### 1. Introduction

Electromagnetic metamaterials with negative permittivity or/and permeability have triggered tremendous fundamental and prac-

tical interest in the past few decades, owing to their exceptional physical properties and intriguing applications, such as invisibility, imaging, antennae, sensors, waveguides, electromagnetic wave absorbers and so on.<sup>1–8</sup> Since Smith *et al.* successfully obtained a negative refractive index in a patterned metamaterial consisting of periodic unit cells in 2000,<sup>9</sup> various patterned metamaterials have been designed and fabricated to achieve negative permittivity or/and permeability at multiple frequency bands.<sup>10–13</sup> In these metamaterials, their unique electromagnetic property mainly derives from the arrangement of their ordered structures, and is dominated by the geometrical parameters of their periodical structure such as size and topology.<sup>14,15</sup> The feasibility of realizing negative electromagnetic parameters was demonstrated in the materials without clear periodic structures.<sup>16–18</sup> These materials are termed random metamaterials and have an isotropic electromagnetic response.<sup>19</sup> The negative parameters of these random metamaterials mainly rely on their composition and microstructure, which opens a way to design metamaterials with more freedom.<sup>17</sup>

In the study of random metamaterials, the metal composites captured more attention than other composites.<sup>20,21</sup> Some metal composites, with metal (for example, Ni, Fe, Ag or Co) particles randomly dispersed in a porous alumina host, were prepared to achieved negative electromagnetic parameters of nearly 1 GHz.<sup>22–25</sup> Negative permittivity was revealed to arise from the plasma oscillation of delocalized electrons in formative metal networks, while negative permeability was caused by the strong diamagnetic response of current loops in metallic networks. Tsutaoka *et al.*<sup>19,26,27</sup> reported tunable negative parameters in copper granular composites at microwave frequency bands, with negative permittivity resulting from low frequency plasmonic states in metal particle clusters, and negative permeability originating from the magnetic resonance of magnetic media. Negative parameters were also observed in the metal alloy composites containing Fe<sub>53</sub>Ni<sub>47</sub>, FeNiMo or Fe<sub>78</sub>Si<sub>9</sub>B<sub>13</sub> particles.<sup>28–30</sup> However, those materials have some limitations, such as poor chemical stability, high dissipative losses and enormous negative value of permittivity.<sup>20</sup>

<sup>a</sup>College of Ocean Science and Engineering, Shanghai Maritime University, Shanghai 201306, P. R. China. E-mail: rhfan@shmtu.edu.cn

<sup>b</sup>College of Chemistry and Chemical Engineering, Henan University, Kaifeng 475004, P. R. China. E-mail: dingtao@henu.edu.cn

<sup>c</sup>Dezhou Meta Research Center of Innovative Materials, Dezhou 253000, P. R. China

<sup>d</sup>Integrated Composites Laboratory (ICL), Department of Chemical & Biomolecular Engineering, University of Tennessee, Knoxville, TN 37996, USA. E-mail: zguo10@utk.edu

<sup>e</sup>Key Laboratory for Liquid-Solid Structural Evolution and Processing of Materials (Ministry of Education), Shandong University, Jinan 250061, P. R. China

†Electronic supplementary information (ESI) available. See DOI: 10.1039/c7nr01516j

Carbon composites with negative parameters have also been reported. For example, Zhong *et al.*<sup>31</sup> realized controllable negative permittivity in a polymer nanocomposite with three dimensional carbon nanofibers (CNFs) networks. Guo *et al.*<sup>32–35</sup> achieved negative permittivity in polymer composites with different carbon structures, including graphene, CNFs and carbon fabrics. Negative permittivity was also observed in amorphous carbon composites consisting of carbon membranes spreading out on the pore walls of the porous dielectric matrices.<sup>20,36</sup> The observed small magnitude of negative permittivity in testing frequency was considered to stem from the moderate carrier concentration in the conductive carbon networks. Meanwhile, negative permittivity behavior was found in CNTs and their polymer composites recently, arising from the low frequency plasmonic state in CNTs.<sup>37–40</sup> As a truly one-dimensional conductive nano-material, CNTs with excellent mechanical and thermal properties can be regarded as good candidates for constructing random metamaterials. As compared with the polymer composites, ceramic composites (such as Al<sub>2</sub>O<sub>3</sub>) possess excellent chemical stability and favorable thermal and mechanical properties, and can be better applied in extreme environments.<sup>25,41</sup> However, literature related to negative parameters of CNTs/ceramic composites is rare.

Herein, alumina nanocomposites with CNTs uniformly dispersed in the alumina matrix were prepared by traditional ceramic technology followed by hot-pressing sintering. The conductivity and radio-frequency dielectric behaviors of these composites were investigated. A percolation phenomenon occurred in the nanocomposites on increasing the MWCNT content. With the MWCNT content reaching the percolation threshold, the nanocomposites also underwent a capacitive-inductive transition and a change of the conductive mechanism. Most importantly, two different types of negative permittivity behaviors were observed in the nanocomposites. These unique behaviors were analyzed using the Lorentz model and Drude model, respectively.

## 2. Experimental

The Al<sub>2</sub>O<sub>3</sub> composites with MWCNT contents of 1 wt% (1.85 vol%), 4 wt% (7.01 vol%), 7 wt% (11.33 vol%), 9 wt% (13.76 vol%), 10 wt% (14.82 vol%) and 12 wt% (18.0 vol%) were prepared by hot-pressing sintering. The Al<sub>2</sub>O<sub>3</sub> powders had an average particle size of 100 nm, and their purity was more than 99.9%. Fig. S1† shows the FESEM images of the powders. The MWCNTs with lengths more than 5 μm and diameters ranging from 10 to 30 nm were obtained from the Shenzhen Nanotech Port Co. Ltd, PR China. Pickling of the MWCNTs with 68% nitric acid for about 3 h at 120 °C was conducted to improve their dispersibility and remove impurities. The FESEM images of the obtained MWCNTs are presented in Fig. S2.† The MWCNTs were shortened by an acid treatment process. The mixtures of Al<sub>2</sub>O<sub>3</sub> powders and acid treated MWCNTs were dispersed into ethanol and ultrasonicated for 30 min. Then the suspensions were magnetically stirred for 24 h. The mixed

powders were dried in an air circulation oven at 80 °C for 24 h, and then sieved with a 200-mesh sieve. Finally, the obtained mixture of powders were sintered by hot pressure sintering with 30 MPa pressure at 1550 °C for 1 h under flowing argon to obtain bulk MWCNT/Al<sub>2</sub>O<sub>3</sub> composites. The Al<sub>2</sub>O<sub>3</sub> ceramic was also prepared by the same sintering process for comparison. The sintered samples were polished to mirror surface, and the final size of the circular sample was Ø 30 mm × 2 mm.

The phase composition of the MWCNTs/Al<sub>2</sub>O<sub>3</sub> composites was measured by an X-ray diffractometer (XRD, XD2/3, Beijing Purkinje General Instrument Co., Ltd, Beijing, China) with Cu K<sub>α</sub> radiation in air at room temperature. The fracture surface morphology and microstructure of the composites were obtained using a field emission scanning electron microscope (FESEM, SU-70, Hitachi, Tokyo, Japan). The electrical properties (including conductivity, impedance and permittivity) of the specimens were determined using an Agilent E4991A Precision Impedance Analyzer with a 16453A dielectric test fixture in a frequency ranging from 10 MHz to 1 GHz. The impedance ( $Z'$ ,  $Z''$ ), capacitance ( $C$ ) and resistance ( $R_p$ ) data of the samples were tested by the impedance analyzer under alternating current (ac) voltage 100 mV at room temperature. The complex permittivity ( $\epsilon'$ ,  $\epsilon''$ ), impedance modulus value ( $|Z|$ ) and the real part of ac conductivity ( $\sigma_{ac}$ ) were calculated by eqn (1)–(4), respectively:

$$\epsilon' = \frac{Cd}{\epsilon_0 S} \quad (1)$$

$$\epsilon'' = \frac{d}{2\pi f \epsilon_0 S R_p} \quad (2)$$

$$|Z| = \sqrt{|Z'|^2 + |Z''|^2} \quad (3)$$

$$\sigma_{ac} = \frac{d}{RS} \quad (4)$$

where  $d$  is the sample thickness,  $S$  is the electrode plate area,  $C$  is the capacitance,  $R_p$  is parallel resistance,  $R$  is the real part of impedance ( $R = Z'$ ),  $\epsilon_0$  is the permittivity of vacuum ( $8.85 \times 10^{-12}$  F m<sup>-1</sup>), and  $f$  is the frequency.

## 3. Results and discussion

### 3.1 Microstructure characterization

Fig. 1 and S3† show the FESEM images of MWCNTs/Al<sub>2</sub>O<sub>3</sub> composites with different MWCNT contents. The isolated nanotubes are uniformly distributed in the alumina matrix and attached to the grains. As the MWCNT content increases, the nanotubes gradually interconnect with each other, and the three-dimensional nanotube networks can be observed in the composites with high MWCNT contents (Fig. 1d and S3d†). Large differences in Al<sub>2</sub>O<sub>3</sub> grain sizes and shapes are also observed in the microscopy images. The MWCNTs act as pinning centers hindering Al<sub>2</sub>O<sub>3</sub> grain growth during sintering. For the samples with high MWCNT concentrations, the enhanced pinning effect leads to a decrease of grain size and a change of grain shape to an ellipsoidal shape. Fig. 2 shows the XRD patterns of MWCNTs

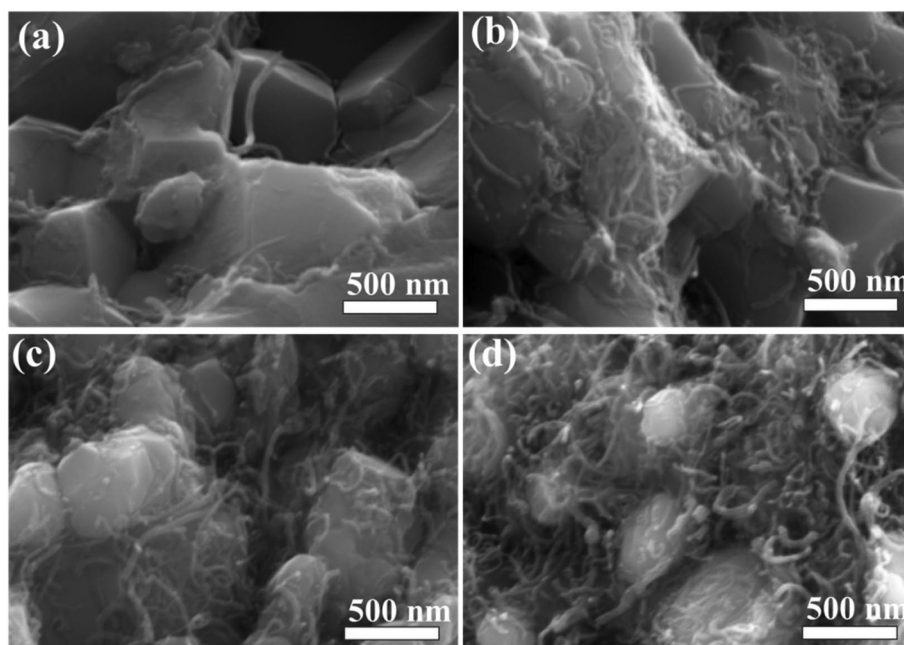


Fig. 1 FESEM images of MWCNTs/ $\text{Al}_2\text{O}_3$  composites with a MWCNT content of (a) 1; (b) 4; (c) 7 and (d) 10 wt%.

and their composites. Two characteristic peaks are observed for MWCNTs at around  $26^\circ$  and  $43^\circ$ .<sup>42,43</sup> But the main crystalline phases of the composites are  $\text{Al}_2\text{O}_3$ , and the characteristic peaks of MWCNTs cannot be clearly identified in the XRD patterns. This may be due to the fact that the MWCNT contents are less, or the intensity of MWCNTs peaks is much lower than those of the crystalline  $\text{Al}_2\text{O}_3$ .

### 3.2 Conductivity behavior

Fig. 3 shows the frequency dependent ac conductivity ( $\sigma_{ac}$ ) for the  $\text{Al}_2\text{O}_3$  ceramic and its composites with different

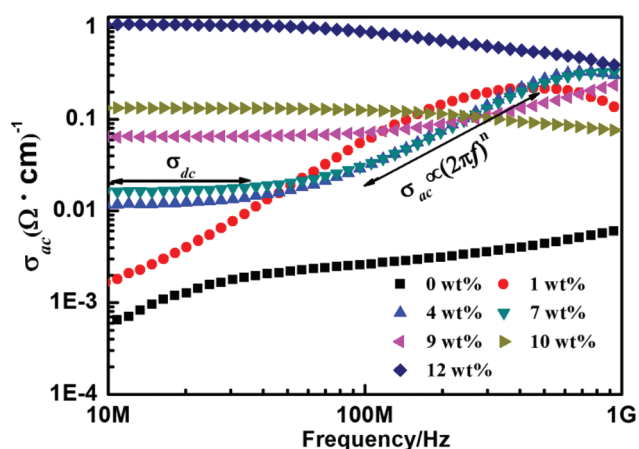


Fig. 3 Frequency dispersions of ac conductivity for the  $\text{Al}_2\text{O}_3$  ceramic and MWCNTs/ $\text{Al}_2\text{O}_3$  composites with different MWCNT contents.

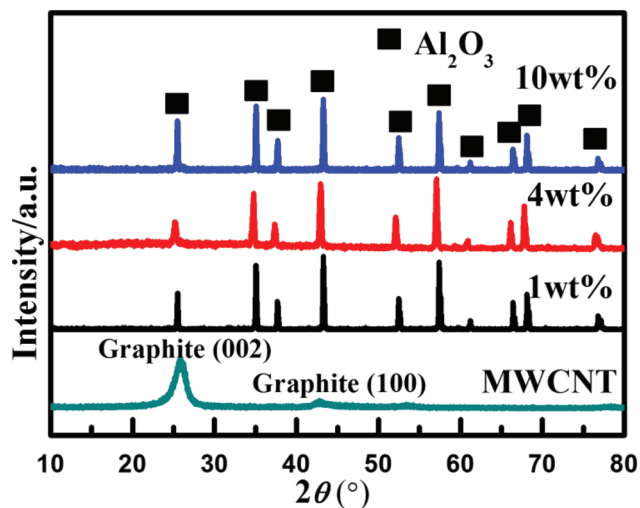


Fig. 2 XRD patterns of MWCNTs and MWCNTs/ $\text{Al}_2\text{O}_3$  composites with different MWCNT contents.

MWCNT contents. The  $\sigma_{ac}$  increases on increasing the frequency of the composites with a content of not more than 10 wt%, while the  $\sigma_{ac}$  decreases as the frequency increases for composites with a high MWCNT content. The different variation trends of  $\sigma_{ac}$  depending on the frequency indicate different conductivity mechanisms, and a percolation phenomenon occurs in the composites on increasing the MWCNT content. The percolation threshold is between 9 wt% (13.76 vol%) and 10 wt% (14.82 vol%). The schematic of microstructural evolution and conductivity mechanisms for the composites with various nanotube contents is shown in Fig. 4. For the composites below the percolation

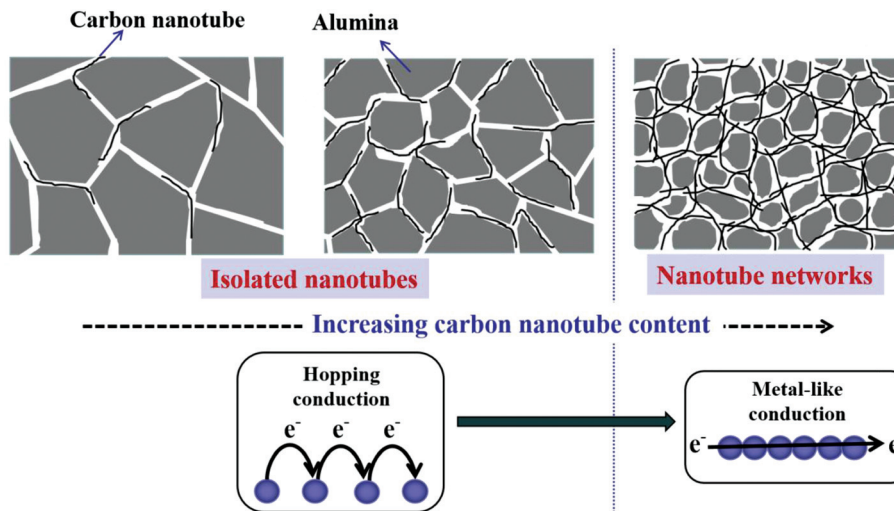


Fig. 4 Microstructural evolution schematic of the MWCNTs/Al<sub>2</sub>O<sub>3</sub> composites on increasing the MWCNT contents.

threshold, the  $\sigma_{ac}$ - $f$  relationship in the low frequency obeys the formula:<sup>23</sup>

$$\sigma_{ac} = \sigma_{dc} + A(2\pi f)^n \quad (5)$$

where  $\sigma_{dc}$  is direct current conductivity,  $f$  is the frequency,  $A$  is the pre-exponential factor and  $n$  is the fractional exponent ( $0 < n < 1$ ). This is suggestive of a hopping conduction behavior in the composites. That is to say, the electrons can “jump” between adjacent MWCNTs under the action of an external electric field.<sup>25</sup> And a deviation from the law in the conductivity spectra at the high frequency should be ascribed to the contribution of dielectric resonance behavior,<sup>44</sup> which we will discuss later. Furthermore, there is no  $\sigma_{dc}$  plateau at low frequency in the conductivity spectrum of the composites with 1 wt% MWCNT content, which should appear in the lower frequency band (below 10 MHz).

When the MWCNT content exceeds the percolation threshold, the nanotubes or tube clusters are connected to each other to form a conducting network throughout the composites, which results in a metal-like conductive behavior.<sup>23,45</sup> As is well known, when an alternating electric current flows through a conductor, the electric current mainly flows at the “skin” of the conductor, which is called the skin effect. The skin depth can be expressed as eqn (6):<sup>25</sup>

$$\delta = \left( \frac{2}{\omega \sigma_{dc} \mu} \right)^{1/2} \quad (6)$$

where  $\delta$  is the skin depth,  $\omega$  is the angular frequency ( $\omega = 2\pi f$ ) and  $\mu$  is the static permeability. The increasing frequency will reduce the skin depth and enhance the skin effects.<sup>23</sup> Hence, the  $\sigma_{ac}$  of composites decreases with increasing the frequency, especially at high frequencies.

### 3.3 Reactance and equivalent circuit analysis

Fig. 5 shows the frequency dependence of reactance ( $Z''$ ) and impedance ( $|Z|$ ) for the pure Al<sub>2</sub>O<sub>3</sub> ceramic and its composites

with different MWCNT contents. Materials which are placed into an external ac electric field can be regarded as a circuit consisting of capacitors, resistors and inductors.<sup>24</sup> In the circuit, the inductor and capacitor will oppose the change of electric field, which is known as inductive reactance ( $Z_L$ ) and capacitive reactance ( $Z_C$ ). The reactance is expressed as  $Z'' = Z_L - Z_C$ .<sup>20</sup> The  $Z''$  increases as the MWCNT content increases, which is attributed to the enhanced inductance resulting from the enhanced connectivity of MWCNTs. The  $Z''$  of the Al<sub>2</sub>O<sub>3</sub> ceramic and its composites with MWCNT contents less than 10 wt% is negative ( $Z'' < 0$ ) in the whole test frequency band (Fig. 5a), indicating that the  $Z_C$  is larger than the  $Z_L$ . The inductance is very weak in the composites with the low MWCNT contents, so the composites can be regarded as a capacitor with leakage current and show a capacitive behavior.<sup>21</sup> On further increasing the MWCNT content, the  $Z''$  becomes positive ( $Z'' > 0$ ) (Fig. 5b), and the composites manifest an inductive behavior, because the inductance is dominant in the composites. There is a shift for  $Z''$  from positive to negative, demonstrating that the composites underwent an inductive–capacitive transition on increasing the frequency.

The equivalent circuit model is used to analyze the impedance response of the composites, Fig. 5c. The values of the corresponding parameters from the fitting results are listed in Table S1.† It is found that the equivalent circuit can model the experimental data very well. The composites with low MWCNT contents are equivalent to a circuit consisting of resistors ( $R_s$  and  $R_p$ ) and a capacitor ( $C$ ) (inset of Fig. 5c).  $R_p$  represents an internal contact resistor resulting from a current through the composites (leakage current), while  $R_s$  is related to the plate and electrode resistance as well as resistance effects due to the operating conditions (such as signal frequency).<sup>46,47</sup> The increase of MWCNT content results in the nanotubes being much closer to each other in the composites, leading to the enhancement of electric leakage. Hence, the  $R_p$  of composites decreases as the MWCNT content increases.<sup>47</sup> And the



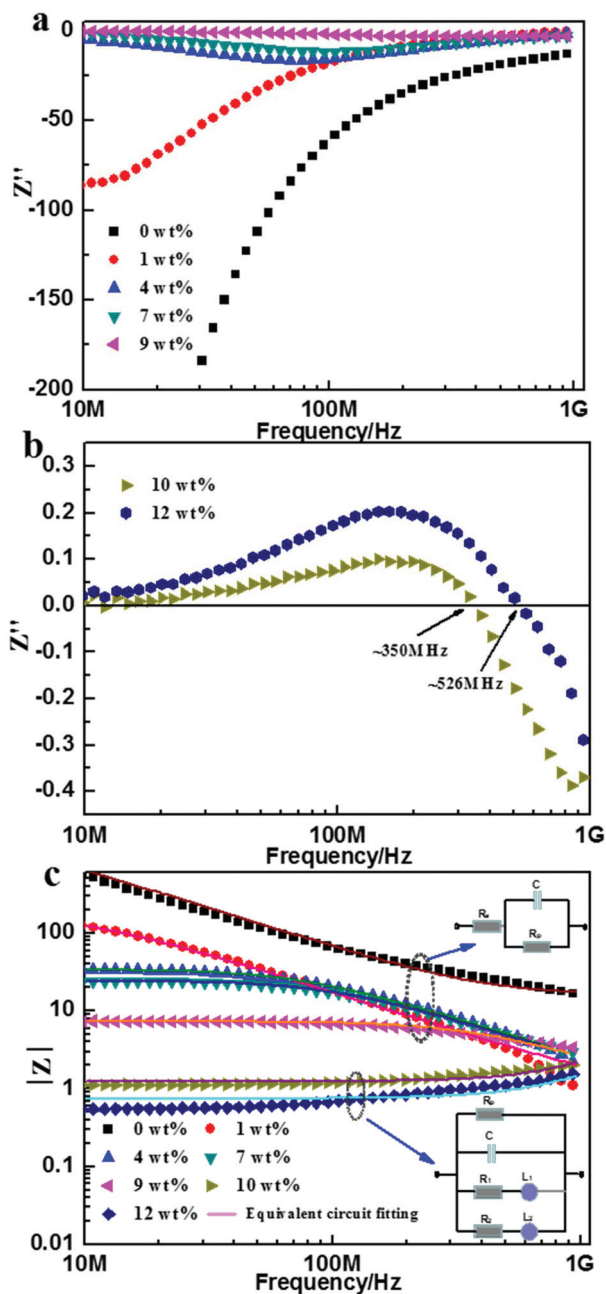


Fig. 5 Frequency dependence of the reactance (a), (b) and impedance (c) for the  $\text{Al}_2\text{O}_3$  ceramic and MWCNTs/ $\text{Al}_2\text{O}_3$  composites with different MWCNT contents. The equivalent circuit models are also shown in (c).

$C$  increases on increasing the nanotube content due to the enlarged MWCNT- $\text{Al}_2\text{O}_3$  interface area.<sup>24</sup> The composites beyond the percolation threshold are equivalent to a circuit consisting of resistors ( $R_p$ ,  $R_1$  and  $R_2$ ), capacitor ( $C$ ), and inductances ( $L_1$  and  $L_2$ ) (inset of Fig. 5c). The introduced inductance element, in the equivalent circuit for the composites with high MWCNT contents, is attributed to the formation of conductive MWCNT networks and the generation of current loops in the conductive networks under the high frequency electric field.<sup>21</sup> As the MWCNT content increases from

10 to 12 wt%, the inductances ( $L_1$  and  $L_2$ ) become larger due to the formation of more nanotube networks in the composites.

### 3.4 Negative permittivity behavior

Fig. 6 depicts the frequency dependences of permittivity ( $\epsilon^* = \epsilon' - i\epsilon''$ ) for the  $\text{Al}_2\text{O}_3$  ceramic and its composites with various contents of MWCNTs. The dielectric curves are clearly different in the composites with different MWCNT contents. The real part of the permittivity ( $\epsilon'$ ) of the composites below the percolation threshold (Fig. 6a) increases with the increase

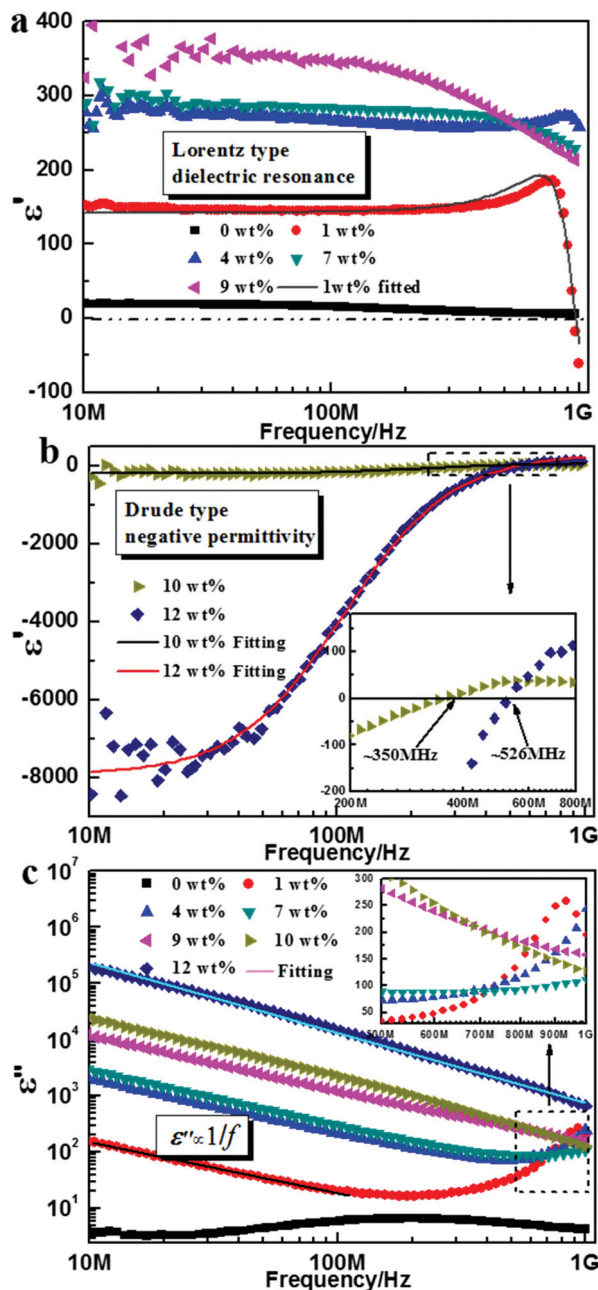


Fig. 6 Frequency dependences of permittivity for the  $\text{Al}_2\text{O}_3$  ceramic and MWCNTs/ $\text{Al}_2\text{O}_3$  composites with different MWCNT contents.

of the MWCNT content, which coincides with the results of the equivalent circuit analysis. A dielectric resonance appears in the composites with low MWCNT contents (for example, 1 wt%) at high frequency, and yet the complete resonance curve is not observed in our testing frequency region. The dielectric resonance behavior is well described by the Lorentz model:<sup>28,48,49</sup>

$$\varepsilon^* = \varepsilon' - i\varepsilon'' = 1 + \frac{\omega_p^2}{\omega_0^2 - \omega^2 + i\Gamma_L\omega} \quad (7)$$

$$\varepsilon' = 1 + \frac{\omega_p^2(\omega_0^2 - \omega^2)}{(\omega_0^2 - \omega^2)^2 + \omega^2\Gamma_L^2} \quad (8)$$

where  $\varepsilon'$  is the real part of permittivity,  $\varepsilon''$  is the imaginary part of permittivity,  $\omega$  ( $\omega = 2\pi f$ ) is the angular frequency of the electric field,  $\omega_0$  ( $\omega_0 = 2\pi f_0$ ) is the characteristic frequency (or resonance frequency),  $\omega_p$  ( $\omega_p = 2\pi f_p$ ) is the angular plasma frequency describing the resonance strength, and  $\Gamma_L$  represents the damping constant related to the broadening of resonance. Excellent agreement between the measured and simulated results was obtained (solid line in Fig. 6a), and the obtained  $\Gamma_L$ ,  $f_p$  and  $f_0$  are  $3 \times 10^9$ , 11.6 and 955 MHz, respectively. The Lorentz type dielectric resonance should result from the induced electric dipole in the isolated MWCNTs.<sup>28</sup> When the frequency of external electric field reaches the resonance frequency range (near  $f_0$ ), negative permittivity may be obtained. For the composites with a loading of 1 wt%, negative permittivity is observed in the resonance frequency band (950 MHz–1 GHz). The composite with 4 wt% MWCNT content also shows the dielectric resonance behavior at high frequency (around 1 GHz), whereas negative permittivity behavior is not observed in the measured frequency band. And it is reasonable to suppose that negative permittivity would appear in the higher frequency band (more than 1 GHz). Moreover, such Lorentz type dielectric resonance and negative permittivity behavior were also observed in many other composites.<sup>28,48,50</sup> In the composites with MWCNT contents of 7 and 9 wt%, the  $\varepsilon'$  decreases on increasing the frequency, which is attributed to the enhanced electric leakage. Along with the increase of MWCNT content, the nanotubes are much closer to each other and more electrons can hop between the neighboring nanotubes, causing enhancement of electric leakage. For the composites beyond the percolation threshold, further increasing the MWCNT content leads to the interconnection of nanotubes, and three-dimensional MWCNT networks are formed. A plasma-like negative permittivity behavior is observed at low frequencies (Fig. 6b), resulting from the low-frequency plasmon of free electrons in MWCNT networks.<sup>39</sup> The dispersion characteristic of permittivity can be explained by the following Drude model:<sup>51,52</sup>

$$\varepsilon^* = \varepsilon' - i\varepsilon'' = \varepsilon_\infty - \frac{\omega_p^2}{\omega^2 + i\omega\Gamma_D} \quad (9)$$

$$\varepsilon' = \varepsilon_\infty - \frac{\omega_p^2}{\omega^2 + \Gamma_D^2} \quad (10)$$

$$\omega_p = \sqrt{\frac{n_{\text{eff}}e^2}{m_{\text{eff}}\varepsilon_0}} \quad (11)$$

where  $n_{\text{eff}}$  is the effective concentration of delocalized electrons,  $m_{\text{eff}}$  is the effective weight of an electron,  $e$  is the electron charge ( $1.6 \times 10^{-19}$  C),  $\varepsilon_0$  is the permittivity of a vacuum ( $8.85 \times 10^{-12}$  F m<sup>-1</sup>),  $\varepsilon_\infty$  is high frequency limit permittivity and  $\Gamma_D$  is the damping constant. The fitting results agree well with the experimental curves of the  $\varepsilon'$ . The fitted  $\varepsilon'$ - $f$  curves are obtained using the iterative method in OriginPro 8 software according to eqn (10). The obtained fitting parameters including  $\Gamma_D$ ,  $\varepsilon_\infty$  and  $f_p$  for composites with 10 wt% MWCNT content are  $3.5 \times 10^9$ , 62 and 3.5 GHz, respectively. For the composites with 12 wt% MWCNTs content, the values of  $\Gamma_D$ ,  $\varepsilon_\infty$  and  $f_p$  are  $6.7 \times 10^8$ , 318.8 and 9.7 GHz, respectively. The  $\varepsilon'$  crosses zero at the screened plasma frequency given by:<sup>51</sup>

$$f_\Omega = \frac{f_p}{\sqrt{\varepsilon_\infty}} \quad (12)$$

Negative permittivity is expected when the frequency is below the screened plasma frequency  $f_\Omega$ . The  $f_\Omega$  of composites with 10 wt% and 12 wt% MWCNT content is around 350 and 526 MHz, respectively. The increasing MWCNT content will lead to the formation of more conductive networks and a higher conductivity, indicating an increase of effective electron concentration  $n_{\text{eff}}$  and a decrease of effective weight of electrons  $m_{\text{eff}}$ .<sup>23</sup> Therefore, according to the Drude model,  $f_p$  and  $f_\Omega$  shift to a higher frequency, and the magnitude of negative permittivity increases in the composites with a higher MWCNT content. As can be noted, the  $f_\Omega$  corresponds well with the frequency points of the negative–positive transitions for  $Z''$ . In some metal composites and single-phase material,<sup>21,23,53,54</sup> similar results were also observed, and an inductance character ( $Z'' > 0$ ) frequently appeared along with negative permittivity behavior. Thus, we believe that the inductive behavior is a characteristic of the negative permittivity phenomenon.<sup>53</sup> The obtained composites have many potential applications. For instance, the composites with the low-frequency plasmon can be regarded as a novel plasmonic sensor in the radio frequency,<sup>6,55,56</sup> and can also be applied in the other sensors.<sup>57–61</sup> The composites present potential for applications in the electromagnetic shielding field, and would show excellent microwave shielding property in the frequency regions where their permittivity is negative.<sup>62–65</sup> Furthermore, the class of materials whose permittivity is near-zero around a given frequency is called epsilon-near-zero metamaterials.<sup>66</sup> These materials provide unconventional properties and fascinating applications, such as super-coupling, cloaking, highly directive antennas and optical devices.<sup>67,68</sup> In this work, when the operating frequency is near  $f_\Omega$ , the  $\varepsilon'$  attains near-zero values, so our obtained composites can be considered as a promising alternative for epsilon-near-zero metamaterials. Moreover, work focusing on epsilon-near-zero behaviors will be carried out in the future.

The  $\varepsilon''$  is known to be useful to evaluate the dielectric loss of materials. In the case of the percolative composite system,

the dielectric loss, which is closely associated with the frequency and concentration of conductive fillers, mainly originates from the conduction process, surface polarization and dipole movement.<sup>69,70</sup> Thus  $\epsilon''$  can be expressed by eqn (13):

$$\epsilon'' = \epsilon''_c + \epsilon''_d + \epsilon''_p \quad (13)$$

where  $\epsilon''_c$  is conduction loss,  $\epsilon''_d$  is dipolar loss and  $\epsilon''_p$  is interfacial polarization related loss. Generally, the interfacial polarization phenomenon occurs at low frequency, which is not more than 1 MHz.<sup>71</sup> Once the frequency of the external electric field reaches a high enough level, the charges do not have time to accumulate at the interface, leading to the disappearance of interfacial polarization. Therefore, the dielectric loss mainly includes the conduction loss and dipolar loss in our test frequency (10 MHz–1 GHz). The conduction loss arises from a leakage current among conductive fillers or the contact resistors in the circuit model, and can be described by:<sup>70</sup>

$$\epsilon''_c = \frac{\sigma_{dc}}{2\pi f \epsilon_0} \quad (14)$$

The  $\sigma_{dc}$  is constant for a given material, so the  $\epsilon''_c$  is inversely related to  $f$  ( $\epsilon''_c \propto f^{-1}$ ). The dipolar loss stems from polarization currents and the movement of dipoles on continuously changing the electric fields.<sup>69</sup>

Fig. 6c presents the  $\epsilon''$  versus frequency for the  $\text{Al}_2\text{O}_3$  ceramic and its composites with different MWCNT contents. The incorporation of MWCNTs leads to an evident increment of  $\epsilon''$ . The  $\epsilon''$  of composites beyond the percolation threshold linearly descends on increasing the frequency, indicating that the conduction loss is dominant in determining the dielectric loss ( $\epsilon'' \approx \epsilon''_c$ ). For the composites under the percolation threshold, the plots of  $\epsilon''$  versus  $f$  exhibit the linear decrease relationship in the low frequency region, and then demonstrate a nonlinear increasing trend at the high frequency region. That is, there is a change of the dominant role in the dielectric loss from the conduction loss to the dipolar loss on increasing the frequency. The results can be understood by the reason that the conductivity loss decreases with increasing the frequency (according to eqn (14)), and the contribution from the dipolar loss becomes more significant at high frequency.<sup>72</sup> It should be noted from the inset of Fig. 6c that a dielectric loss peak is observed along with the Lorentz type dielectric resonance in the composites with 1 wt% MWCNT content. Meanwhile, for the composites with MWCNT content increasing from 1 to 9 wt%, the loss peaks should move toward the higher frequency which exceeds the tested frequency band.

## 4. Conclusion

Alumina nanocomposites with MWCNT concentrations between 1 and 12 wt% were fabricated by hot-pressing sintering. It was found that MWCNTs were uniformly dispersed in the  $\text{Al}_2\text{O}_3$  matrixes. The electrical conductivity studies revealed that a percolation phenomenon occurred in the composites,

accompanied by a change in the conductive mechanism from hopping conduction to metal-like conduction, owing to the formation of conductive MWCNT networks. Meanwhile, equivalent circuit models for the composites were proposed through analyzing the impedance spectra. Two types of negative permittivity behaviors were observed in the composites on increasing the MWCNT content. The resonance-induced negative permittivity behavior could be fitted well by the Lorentz model and originated from the induced electric dipole in the isolated nanotubes. As the MWCNT content reached the percolation threshold, the composites showed plasma-like negative permittivity behavior, which resulted from the low frequency plasmonic state produced by the conductive MWCNT networks. This work has possible profound implications for exploring the generation and regulation mechanism of negative permittivity behavior. The obtained carbon nanotube composites can be regarded as promising candidates for random metamaterials, and can find potential applications in electromagnetic shielding, novel antennae and sensors.

## Acknowledgements

The authors acknowledge the support of the National Basic Research Program of China (973 Program, No. 2014CB643306), National Natural Science Foundation of China (Grant No. 51602194, 51602195, 51402170), the Science and Technology Development Program of Henan Province (172102410028), and the Natural Science Foundation of Shandong Province (No. ZR2016EMM09). C. Cheng acknowledges the support from the China Scholarship Council.

## Notes and references

- 1 T. Ergin, N. Stenger, P. Brenner, J. B. Pendry and M. Wegener, *Science*, 2010, **328**, 337–339.
- 2 M. Wiltshire, J. Pendry, I. Young, D. Larkman, D. Gilderdale and J. Hajnal, *Science*, 2001, **291**, 849–851.
- 3 B. J. Roxworthy and K. C. Toussaint, *Nanoscale*, 2014, **6**, 2270–2274.
- 4 A. Moreau, C. Ciraci, J. J. Mock, R. T. Hill, Q. Wang, B. J. Wiley, A. Chilkoti and D. R. Smith, *Nature*, 2012, **492**, 86–89.
- 5 Y. Hou, *Nanoscale*, 2012, **4**, 874–878.
- 6 W. Tang, L. Wang, X. Chen, C. Liu, A. Yu and W. Lu, *Nanoscale*, 2016, **8**, 15196–15204.
- 7 E. J. Smith, Z. Liu, Y. Mei and O. G. Schmidt, *Nano Lett.*, 2009, **10**, 1–5.
- 8 S. Song, Q. Chen, L. Jin and F. Sun, *Nanoscale*, 2013, **5**, 9615–9619.
- 9 D. R. Smith, W. J. Padilla, D. Vier, S. C. Nemat-Nasser and S. Schultz, *Phys. Rev. Lett.*, 2000, **84**, 4184.
- 10 H. Chen, *J. Mater. Chem.*, 2011, **21**, 6452–6463.
- 11 Q. Zhao, J. Zhou, F. Zhang and D. Lippens, *Mater. Today*, 2009, **12**, 60–69.



- 12 Q. Zhao, L. Kang, B. Du, B. Li, J. Zhou, H. Tang, X. Liang and B. Zhang, *Appl. Phys. Lett.*, 2007, **90**, 011112.
- 13 E. S. P. Leong, Y. J. Liu, J. Deng, Y. T. Fong, N. Zhang, S. J. Wu and J. H. Teng, *Nanoscale*, 2014, **6**, 11106–11111.
- 14 A. Zhukov, *Novel Functional Magnetic Materials: Fundamentals and Applications*, Springer, 2016.
- 15 X. Zhao, C. Yuan, L. Zhu and J. Yao, *Nanoscale*, 2016, **8**, 15273–15280.
- 16 K. Hur, Y. Francescato, V. Giannini, S. A. Maier, R. G. Hennig and U. Wiesner, *Angew. Chem., Int. Ed.*, 2011, **50**, 11985–11989.
- 17 Z. C. Shi, R. H. Fan, Z. D. Zhang, K. L. Yan, X. H. Zhang, K. Sun, X. F. Liu and C. G. Wang, *J. Mater. Chem. C*, 2013, **1**, 1633–1637.
- 18 J. Zhu, S. Wei, N. Haldolaarachchige, J. He, D. P. Young and Z. Guo, *Nanoscale*, 2012, **4**, 152–156.
- 19 T. Tsutaoka, T. Kasagi, S. Yamamoto and K. Hatakeyama, *Appl. Phys. Lett.*, 2013, **102**, 181904.
- 20 C. Cheng, R. Fan, L. Qian, X. Wang, L. Dong and Y. Yin, *RSC Adv.*, 2016, **6**, 87153–87158.
- 21 Z. C. Shi, S. G. Chen, K. Sun, X. Wang, R. H. Fan and X. A. Wang, *Appl. Phys. Lett.*, 2014, **104**, 252908.
- 22 Z. C. Shi, R. H. Fan, Z. D. Zhang, L. Qian, M. Gao, M. Zhang, L. T. Zheng, X. H. Zhang and L. W. Yin, *Adv. Mater.*, 2012, **24**, 2349–2352.
- 23 Z. C. Shi, R. H. Fan, K. L. Yan, K. Sun, M. Zhang, C. G. Wang, X. F. Liu and X. H. Zhang, *Adv. Funct. Mater.*, 2013, **23**, 4123–4132.
- 24 Z. Shi, R. Fan, Z. Zhang, H. Gong, J. Ouyang, Y. Bai, X. Zhang and L. Yin, *Appl. Phys. Lett.*, 2011, **99**, 032903.
- 25 X. A. Wang, Z. C. Shi, M. Chen, R. H. Fan, K. L. Yan, K. Sun, S. B. Pan and M. X. Yu, *J. Am. Ceram. Soc.*, 2014, **97**, 3223–3229.
- 26 T. Tsutaoka, T. Kasagi, S. Yamamoto and K. Hatakeyama, *J. Magn. Magn. Mater.*, 2015, **383**, 139–143.
- 27 T. Tsutaoka, K. Fukuyama, H. Kinoshita, T. Kasagi, S. Yamamoto and K. Hatakeyama, *Appl. Phys. Lett.*, 2013, **103**, 261906.
- 28 T. Tsutaoka, H. Massango, T. Kasagi, S. Yamamoto and K. Hatakeyama, *Appl. Phys. Lett.*, 2016, **108**, 191904.
- 29 M. Chen, M. Gao, F. Dang, N. Wang, B. Zhang and S. Pan, *Ceram. Int.*, 2016, **42**, 6444–6449.
- 30 Q. Hou, K. L. Yan, R. H. Fan, Z. D. Zhang, M. Chen, K. Sun and C. B. Cheng, *RSC Adv.*, 2015, **5**, 9472–9475.
- 31 B. Li, G. Sui and W. H. Zhong, *Adv. Mater.*, 2009, **21**, 4176–4180.
- 32 J. Zhu, X. Zhang, N. Haldolaarachchige, Q. Wang, Z. Luo, J. Ryu, D. P. Young, S. Wei and Z. Guo, *J. Mater. Chem.*, 2012, **22**, 4996–5005.
- 33 J. Zhu, H. Gu, Z. Luo, N. Haldolaarachchige, D. P. Young, S. Wei and Z. Guo, *Langmuir*, 2012, **28**, 10246–10255.
- 34 J. Zhu, S. Wei, J. Ryu and Z. Guo, *J. Phys. Chem. C*, 2011, **115**, 13215–13222.
- 35 B. Qiu, J. Guo, Y. Wang, X. Wei, Q. Wang, D. Sun, M. A. Khan, D. P. Young, R. O'Connor and X. Huang, *J. Mater. Chem. C*, 2015, **3**, 3989–3998.
- 36 C. Cheng, K. Yan, R. Fan, L. Qian, Z. Zhang, K. Sun and M. Chen, *Carbon*, 2016, **96**, 678–684.
- 37 Y. Sun, J. Wang, S. Qi, G. Tian and D. Wu, *Appl. Phys. Lett.*, 2015, **107**, 012905.
- 38 X. Zhang, X. Yan, Q. He, H. Wei, J. Long, J. Guo, H. Gu, J. Yu, J. Liu and D. Ding, *ACS Appl. Mater. Interfaces*, 2015, **7**, 6125–6138.
- 39 M. Lin, D. Chuu and K. K. Shung, *Phys. Rev. B: Condens. Matter*, 1997, **56**, 1430.
- 40 H. Gu, J. Guo, Q. He, Y. Jiang, Y. Huang, N. Haldolaarachchige, Z. Luo, D. P. Young, S. Wei and Z. Guo, *Nanoscale*, 2014, **6**, 181–189.
- 41 J. Gangwar, B. K. Gupta, S. K. Tripathi and A. K. Srivastava, *Nanoscale*, 2015, **7**, 13313–13344.
- 42 H. Liu, J. Gao, W. Huang, K. Dai, G. Zheng, C. Liu, C. Shen, X. Yan, J. Guo and Z. Guo, *Nanoscale*, 2016, **8**, 12977–12989.
- 43 Y. S. Tang, J. Kong, J. W. Gu and G. Z. Liang, *Polym.–Plast. Technol. Eng.*, 2009, **48**, 359–366.
- 44 C. Homes, T. Vogt, S. Shapiro, S. Wakimoto and A. Ramirez, *Science*, 2001, **293**, 673–676.
- 45 X. Yan, J. Gu, G. Zheng, J. Guo, A. M. Galaska, J. Yu, M. A. Khan, L. Sun, D. P. Young, Q. Zhang, S. Wei and Z. Guo, *Polymer*, 2016, **103**, 315–327.
- 46 Y. Xi, Y. Bin, C. Chiang and M. Matsuo, *Carbon*, 2007, **45**, 1302–1309.
- 47 J. Zhang, M. Mine, D. Zhu and M. Matsuo, *Carbon*, 2009, **47**, 1311–1320.
- 48 K. L. Yan, R. H. Fan, M. Chen, K. Sun, L. W. Yin, H. Li, S. B. Pan and M. X. Yu, *J. Alloys Compd.*, 2015, **628**, 429–432.
- 49 M. Dressel and G. Guner, *Electrodynamics of Solids: Optical Properties of Electrons in Matter*, Cambridge University Press, Cambridge, 2002.
- 50 A. N. Lagarkov, S. M. Matytsin, K. N. Rozanov and A. K. Sarychev, *J. Appl. Phys.*, 1998, **84**, 3806–3814.
- 51 K. Lee, S. Cho, S. H. Park, A. Heeger, C. W. Lee and S. H. Lee, *Nature*, 2006, **441**, 65–68.
- 52 H. Gu, J. Guo, M. A. Khan, D. P. Young, T. Shen, S. Wei and Z. Guo, *Phys. Chem. Chem. Phys.*, 2016, **18**, 19536–19543.
- 53 K. L. Yan, R. H. Fan, Z. C. Shi, M. Chen, L. Qian, Y. L. Wei, K. Sun and J. Li, *J. Mater. Chem. C*, 2014, **2**, 1028–1033.
- 54 Z. C. Shi, R. H. Fan, X. A. Wang, Z. D. Zhang, L. Qian, L. W. Yin and Y. J. Bai, *J. Eur. Ceram. Soc.*, 2015, **35**, 1219–1225.
- 55 Y. Cui, J. Sun, Y. He, Z. Wang and P. Wang, *Appl. Phys. Lett.*, 2013, **103**, 062906.
- 56 A. V. Kabashin, P. Evans, S. Pastkovsky, W. Hendren, G. A. Wurtz, R. Atkinson, R. Pollard, V. A. Podolskiy and A. V. Zayats, *Nat. Mater.*, 2009, **8**, 867–871.
- 57 H. Liu, M. Dong, W. Huang, J. Gao, K. Dai, J. Guo, G. Zheng, C. Liu, C. Shen and Z. Guo, *J. Mater. Chem. C*, 2017, **5**, 73–83.
- 58 H. Jin, Q. Chen, Z. Chen, Y. Hu and J. Zhang, *CAAI Trans. Intell. Technol.*, 2016, **1**, 104–113.



- 59 H. Liu, Y. Li, K. Dai, G. Zheng, C. Liu, C. Shen, X. Yan, J. Guo and Z. Guo, *J. Mater. Chem. C*, 2015, **4**, 157–166.
- 60 X. Zhang, H. Gao, M. Guo, G. Li, Y. Liu and D. Li, *CAAI Trans. Intell. Technol.*, 2016, **1**, 4–13.
- 61 C. Alippi, *CAAI Trans. Intell. Technol.*, 2016, **1**, 1–3.
- 62 X. Yin, L. Kong, L. Zhang, L. Cheng, N. Travitzky and P. Greil, *Int. Mater. Rev.*, 2014, **59**, 326–355.
- 63 Q. Yuchang, W. Qinlong, L. Fa and Z. Wancheng, *J. Mater. Chem. C*, 2016, **4**, 4853–4862.
- 64 L. Chen, X. Yin, X. Fan, M. Chen, X. Ma, L. Cheng and L. Zhang, *Carbon*, 2015, **95**, 10–19.
- 65 X. Liu, X. Yin, G. Zheng, Y. Liu, L. Kong, Q. Li and X. Yuan, *Ceram. Int.*, 2014, **40**, 531–540.
- 66 N. Engheta, *Science*, 2013, **340**, 286–287.
- 67 B. Edwards, A. Alù, M. E. Young, M. Silveirinha and N. Engheta, *Phys. Rev. Lett.*, 2008, **100**, 033903.
- 68 Y. C. Jun, J. Reno, T. Ribaudo, E. Shaner, J. J. Greffet, S. Vassant, F. Marquier, M. Sinclair and I. Brener, *Nano Lett.*, 2013, **13**, 5391–5396.
- 69 Y. Feng, W. Li, Y. Hou, Y. Yu, W. Cao, T. Zhang and W. Fei, *J. Mater. Chem. C*, 2015, **3**, 1250–1260.
- 70 C. Wu, X. Huang, X. Wu, L. Xie, K. Yang and P. Jiang, *Nanoscale*, 2013, **5**, 3847–3855.
- 71 C. W. Nan, Y. Shen and J. Ma, *Annu. Rev. Mater. Res.*, 2010, **40**, 131–151.
- 72 J. Gu, Z. Lv, Y. Wu, Y. Guo, L. Tian, H. Qiu, W. Li and Q. Zhang, *Composites, Part A*, 2016, **94**, 209–216.